JACS
JOURNAL OF THE AMERICAN CHEMICAL SOCIETY

Article

pubs.acs.org/JACS

Identification of Highly Active Fe Sites in (Ni,Fe)OOH for Electrocatalytic Water Splitting

Daniel Friebel,*[,†,§,¶] Mary W. Louie,[†,‡,¶] Michal Bajdich,[§,¶] Kai E. Sanwald,[§,∥] Yun Cai,[†,‡] Anna M. Wise,[⊥] Mu-Jeng Cheng,[†,‡] Dimosthenis Sokaras,[⊥] Tsu-Chien Weng,[⊥] Roberto Alonso-Mori,[#] Ryan C. Davis,[⊥] John R. Bargar,[⊥] Jens K. Nørskov,[§] Anders Nilsson,[†,§,⊥] and Alexis T. Bell*[,†,‡]

[†]Joint Center for Artificial Photosynthesis, Lawrence Berkeley National Laboratory, 1 Cyclotron Road, Mail Stop 976, Berkeley, California 94720, United States

[‡]Department of Chemical and Biomolecular Engineering, University of California at Berkeley, 107 Gilman Hall, Berkeley, California 94720, United States

[§]SUNCAT Center for Interface Science and Catalysis, SLAC National Accelerator Laboratory, 2575 Sand Hill Road, Menlo Park, California 94025, United States

[∥]Department of Chemistry, Technische Universität München, Lichtenbergstraße 4, 85749 Garching, Germany

[⊥]Stanford Synchrotron Radiation Lightsource, SLAC National Accelerator Laboratory, 2575 Sand Hill Road, Menlo Park, California 94025, United States

[#]Linac Coherent Lightsource, SLAC National Accelerator Laboratory, 2575 Sand Hill Road, Menlo Park, California 94025, United States

Supporting Information

ABSTRACT: Highly active catalysts for the oxygen evolution reaction (OER) are required for the development of photoelectrochemical devices that generate hydrogen efficiently from water using solar energy. Here, we identify the origin of a 500-fold OER activity enhancement that can be achieved with mixed (Ni,Fe)oxyhydroxides ($Ni_{1-x}Fe_xOOH$) over their pure Ni and Fe parent compounds, resulting in one of the most active currently known OER catalysts in alkaline electrolyte. Operando X-ray absorption spectroscopy (XAS) using high energy resolution fluorescence detection (HERFD) reveals that Fe^{3+} in $Ni_{1-x}Fe_xOOH$ occupies octahedral sites with unusually short Fe−O bond distances, induced by edge-sharing with surrounding [NiO_6] octahedra. Using computational methods, we establish that this structural motif results in near optimal adsorption energies of OER intermediates and low overpotentials at Fe sites. By contrast, Ni sites in $Ni_{1-x}Fe_xOOH$ are not active sites for the oxidation of water.

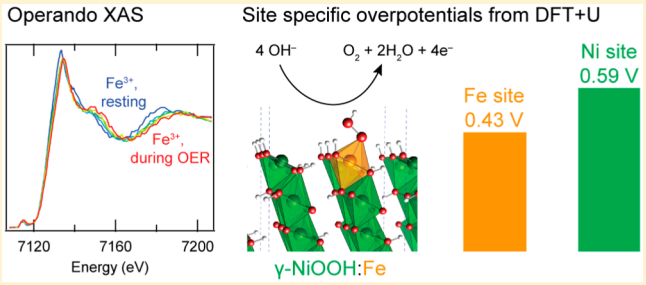

INTRODUCTION

The conversion of solar energy to renewable fuels is an important and scientifically challenging issue. A critical requirement for achieving this goal is an efficient means for photoelectrochemically splitting water to hydrogen and oxygen. The hydrogen can be used to provide fuel for a fuel cell, as a green, carbon-free reducing agent for upgrading of biomass to fuels, or, in the future, for reducing CO_2 to fuels. Prior work has shown that one of the most significant performance losses of electrochemical and photoelectrochemical cells used for the water splitting is due to the high overpotential (>0.35 V) of existing water oxidation catalysts required for the anode of such cells.[1−11] If the overpotential for the oxygen evolution reaction (OER) cannot be reduced, then high band gap photoabsorbers or high catalyst loadings will be needed in order to match geometric photocurrent and catalytic current densities.[1,12] Increased catalyst loading is undesirable since light absorption in the catalyst will reduce the photon flux to the photoabsorber.[13,14] To overcome this limitation, it is necessary to understand what limits the OER activity of existing OER catalysts.

The most promising OER catalysts based on earth-abundant elements are mixed Ni−Fe compounds, which perform best in alkaline eletrolytes.[15−27] While there is consensus that the coexistence of Ni and Fe is required to achieve high activity, a variety of views have been reported regarding the structure of the active phase and whether Fe or Ni constitutes the active center, and only a few studies have examined the energetics of intermediates involved in the OER.[26,28] In an effort to identify the structure of active Ni−Fe OER catalysts, we have used in situ Raman spectroscopy to characterize electrochemically

Received: November 17, 2014
Published: January 5, 2015

DOI: 10.1021/ja511559d
J. Am. Chem. Soc. 2015, 137, 1305−1313

grown Ni−Fe films.[23] This work has shown that NiOOH is present for films containing up to ∼50% Fe, and at higher Fe concentrations there is increasing evidence for a mixture of FeOOH and Fe_2O_3. However, neither this work nor other studies have identified the local structure of the Fe sites unambiguously.[29−32] It is, therefore, desirable to obtain a fundamental understanding of the interactions of Ni and Fe and how they contribute to the high OER activity of Ni−Fe catalysts. A question of particular interest is whether the substitution of Fe cations into NiOOH enhance the OER activity of Ni, Fe, or both, and whether the substitution of Ni into FeOOH can enhance the activity of this phase and if so, how. Answers to these questions would not only explain the unusually high activity of Ni−Fe OER catalysts but should also provide guidance for the design of new catalysts.

Here, we probe the short-range structure at Fe and Ni sites in electrodeposited (Ni,Fe) oxyhydroxide catalysts, across the entire composition range, in 0.1 M KOH with element-sensitive operando X-ray absorption spectroscopy (XAS) in the high energy resolution fluorescence detection (HERFD) mode. The HERFD technique provides detailed electronic structure information through spectra with partially removed core-hole lifetime broadening[33,34] and enhanced pre-edge features.[35,36] XAS analysis, reinforced by density-functional theory with Hubbard U (DFT+U) calculations conducted on model catalysts, leads to the conclusion that electrodeposited (Ni,Fe) oxyhydroxide catalysts contain two phases, Fe-containing γ-NiOOH and γ-FeOOH containing little or no Ni (see Figure 1). DFT+U calculations reveal the effects of catalyst composition on the OER overpotential: the active sites in $Ni_{1-x}Fe_xOOH$ are Fe cations; the alteration of their electronic properties due to incorporation into γ-NiOOH dramatically changes the chemical bonding of these cations with intermediates involved in the OER, resulting a lower OER overpotential and, correspondingly, increased OER activity.

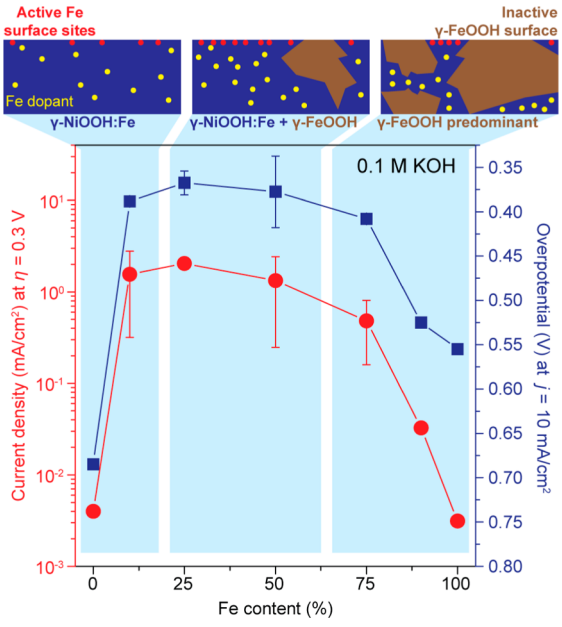

Figure 1. Measured OER activity of mixed Ni−Fe catalysts as a function of Fe content in 0.1 M KOH. For 0% Fe, measurements were performed in electrolyte which was carefully purified to remove any Fe contamination. Top: a schematic illustrating the influence of Fe content on the competing formation of highly active Fe sites in γ-NiOOH and of phase-separated low-activity γ-FeOOH.

EXPERIMENTAL SECTION

All operando XAS measurements were carried out using custom-made spectroelectrochemical cells. Each working electrode consisted of a 1 μm thin silicon nitride window (5 × 5 mm^2 on a 10 × 10 mm^2, 200 μm thick silicon supporting frame) onto which a Ti adhesion layer (4 nm) followed by the Au layer (10 nm) were evaporated (see Supporting Information S1 for details). Ni−Fe catalysts were electrodeposited using the procedure described previously[23] except with a shorter deposition time of 20 s; this prevented the formation of metallic Ni and Fe byproducts that were detected in thicker films (see Supporting Information S2). An intermediate film thickness was prepared for the complementary EXAFS characterization of the catalyst containing 25% Fe; in this case, sputter deposition was used instead of electrodeposition, and the resulting ∼2 nm thick metallic film was subsequently oxidized in 0.1 M KOH by cycling the potential between 0.92 and 1.62 V for ∼17 h at a sweep rate of 10 mV/s. After this treatment no metallic Fe or Ni was detected, and the thickness of the oxidized film (∼10 nm, estimated using the density of the Ni(II)/Fe(III) layered double hydroxide structure[31] at low potential) was sufficient for conventional EXAFS measurements.

During operando XAS measurements, a three-electrode setup using a Pt counter electrode (DOE Business Center for Precious Metals Sales and Recovery, USA) and a Hg/HgO/1 M KOH reference electrode (ET072, CH Instruments, USA) was controlled with a potentiostat (VSP/Z-01, BioLogic, France). All potentials were corrected at 95% for the ohmic drop, which was determined using an AC impedance measurement, and are converted and reported with respect to the reversible hydrogen electrode (RHE).

All XAS measurements were carried out at the Stanford Synchrotron Radiation Lightsource (SSRL). The sample cells were aligned such that both incident beam and fluorescence would enter and exit through the silicon nitride window at the back of the Au electrode at an angle of ∼45°, with no penetration of electrolyte necessary. HERFD XAS measurements were made with the high-resolution spectrometer at SSRL beamline 6−2.[37] The incident energy was selected using a double-crystal monochromator with Si(311) and Si(111) crystals for measurements at the Fe and Ni K-edge, respectively. A Rowland circle spectrometer (R = 1 m) was aligned to the peaks of the Fe and Ni Kα lines. To collect the Fe Kα emission, four spherically bent Ge(440) crystals were aligned to the peak at 6404 eV, corresponding to a Bragg angle of 75.5°. The Ni Kα emission at 7478 eV was collected using three spherically bent Si(620) crystals at a Bragg angle of 74.9°. The combined resolution of spectrometer and monochromator was determined to be 1.0 and 1.3 eV for measurements at the Fe and Ni K-edge, respectively.

HERFD XAS scans were treated by subtracting a constant background (typically ∼25 counts/s) and normalized to an edge-jump of 1. Complementary operando EXAFS measurements were carried out at SSRL beamline 4−1, using a 32-element Ge array detector. In these conventional fluorescence detection measurements the background from elastic and Compton scattering was reduced using a combination of Z-1 filters (3 absorption lengths of Mn (Co) for Fe (Ni) K-edge spectra) with Soller slits. EXAFS data were averaged and normalized using SIXPack[38] and spline-fitted using IFEFFIT[39] through the Athena graphical user interface.[40] EXAFS scattering paths were calculated with FEFF6[41] through the Artemis graphical user interface,[40] using published crystallographic information for γ-FeOOH[42] and γ-NiOOH.[43] Least-squares fitting of the Fourier-transformed EXAFS signals was carried out using IFEFFIT[39] through the SIXPack graphical user interface.[38] All EXAFS data were fitted to the Fourier transforms of $\chi(k)$ using k-weights of 1, 2, and 3 simultaneously.

COMPUTATIONAL METHODS

Bulk and surface properties and energetics of NiFe-oxides were obtained using the GGA-DFT plus Hubbard-U framework (GGA

DOI: 10.1021/ja511559d
J. Am. Chem. Soc. 2015, 137, 1305−1313

+U).[44−46] The RPBE[47] parametrization of GGA was chosen together with rotationally invariant implemetation[48] of Hubbard-*U* term fixed at U_{Hub}(Ni) = 6.6 eV and U_{Hub}(Fe) = 3.5 eV as obtained within linear response theory[49] on respective pure systems. Furthermore, ultrasoft pseudopotentials[50] and plane-wave basis set cutoff of 40 and 400 Ry for density were employed within the PWscf program of the Quantum Espresso package.[51] For periodic slab calculations, slabs of four metal−oxygen layers, separated by at least 16 Å of vacuum and containing 4 metal sites per surface unit mesh and a 4 × 4 × 1 Monkhorst−Pack K-point grid were constructed. The atomic positions within the topmost two layers of the slabs were allowed to relax below a maximum threshold force of 0.05 eV/Å. Additional computational details are given in the Supporting Information (S3−S5).

RESULTS AND DISCUSSION

Catalyst layers, ∼1.8 nm thick, were electrodeposited from $FeSO_4$ and $NiSO_4$ solutions (Supporting Information S1). Figure 1 shows that the addition of Fe to NiOOH results in up to 500-fold higher OER current density compared to pure Ni and Fe oxyhydroxide films (see Supporting Information S6 for details of OER activity measurements). The trend is very similar to results presented earlier;[23] however, a notable exception is the point for no added Fe. Previous measurements of relatively high OER activity for "pure" NiOOH[27] were due to unintentional contamination with trace amounts of Fe present in the electrolyte.[21] After eliminating these impurities (see Supporting Information S7), pure NiOOH films exhibited similar or lower OER activity than pure FeOOH.

In order to understand how the composition-dependent trend in Figure 1 correlates with the local structure at Fe and Ni sites within the catalysts, we acquired Fe and Ni K-edge HERFD XAS over the full range of Fe/Ni ratios and potentials both below and well within conditions where significant OER activity can be observed. The spectra were examined using an analysis of (i) local symmetry induced multiplet structure and relative intensity of the $1s \rightarrow 3d$ transitions in the pre-edge region,[35,52] (ii) oxidation-state sensitive energy positions of the pre-edge centroid[35,52] and photoionization threshold, (iii) structure (bond length) sensitive energy positions of peaks and dips in the high energy range that can be understood in the context of extended X-ray absorption fine structure (EXAFS) and (iv) spectral fingerprinting using literature data and own measurements of well-defined reference compounds. The key results are shown in Figure 2 and Figure 3 (see Supporting Information S8 for the complete set of spectra).

In an OER catalyst containing only Fe sites, the short-range structure closely resembles γ-FeOOH (Figure 2a); however, a small discrepancy can be seen in the pre-edge region at ∼7115 eV, where Fe^{3+} in octahedral coordination is expected to give rise to a characteristic double-peak structure, as observed with γ-FeOOH.[35,52] A small amount (10 ± 3%) of tetrahedrally coordinated Fe^{3+} may therefore exist in addition to a majority species (90 ± 3%) of Fe^{3+} in an octahedral environment (see Supporting Information S9 for a more detailed analysis).

HERFD XAS measurements at potentials (vs reversible hydrogen electrode, RHE) of 1.12, 1.52, 1.62, and 1.72 V (Figure 2a) do not indicate any potential-induced phase transformation in the pure FeOOH sample. By contrast, the Fe *K*-edge HERFD XAS for a sample containing 25% Fe and 75% Ni shows strong potential-induced changes (Figure 2b), which coincide with changes in complementary Ni K-edge HERFD XAS measurements. The latter can be identified with the well-known spectral signatures of α-$Ni(OH)_2$ at low potentials and γ-NiOOH at high potentials.[9,32,53−56] Both α-$Ni(OH)_2$ and γ-NiOOH form layered structures in which sheets of edge-sharing $[NiO_6]$ octahedra are separated by intercalated water molecules and hydrated ions (Figure 2d).[56] The Ni−O bond lengths[9,32,53−56] differ significantly between 2.05 Å in Ni(II)-containing α-$Ni(OH)_2$, and 1.88 Å in γ-NiOOH, which is nonstoichiometric ($NiOOH_{1-x}$) and contains a mixture of Ni(III) and Ni(IV) sites.[57] The significant shift of both the pre-edge peak and the main absorption edge in the Ni K-edge spectra (Figure 2e) shows nearly complete oxidation of Ni sites

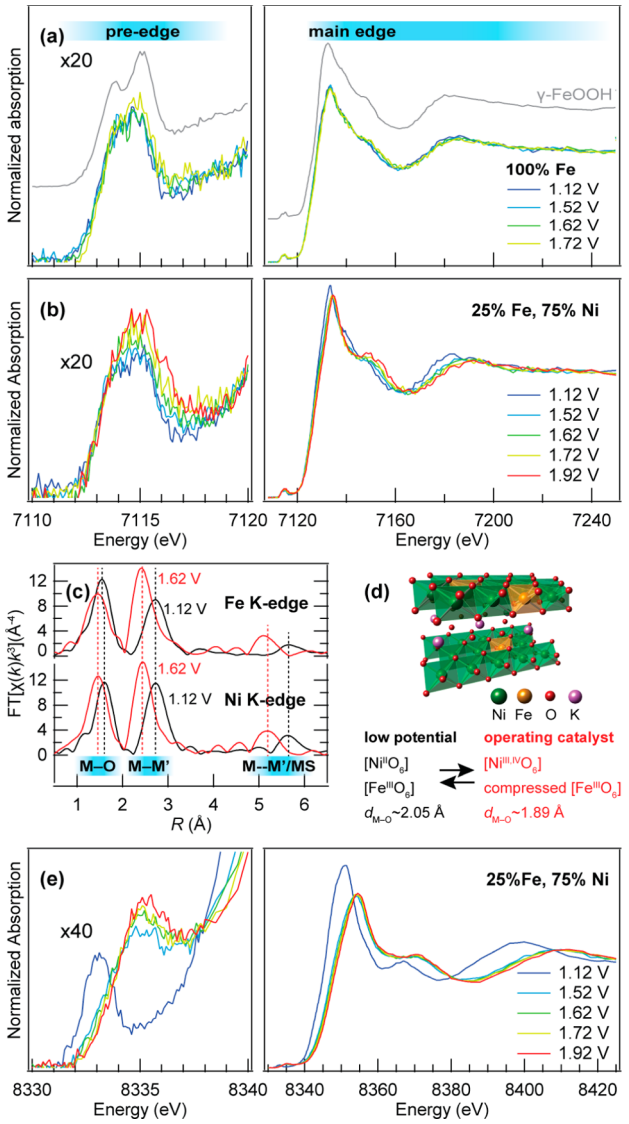

Figure 2. Comparison of 100% Fe-containing sample with OER catalyst containing 25% Fe and 75% Ni using operando HERFD XAS. (a) Catalyst containing 100% Fe. The spectrum of γ-FeOOH is also shown for comparison. Plots of both pre-edge (enlarged) and the full spectra are shown. (b−e) Catalyst containing 25% Fe and 75% Ni. (b) Fe K-edge. While the potential increase does not influence the oxidation-state-sensitive energy of the main absorption threshold (7125 eV), significant Fe−O bond contraction with increasing potential is clearly indicated by the changes of the photoelectron scattering features (energy range above 7140 eV). (c) Complementary operando EXAFS measurement confirming the potential-induced bond contraction at both Fe and Ni sites. (d) Structure model of Fe-doped γ-NiOOH. (e) Ni K-edge XAS showing shifts in both oxidation-state-sensitive and structure-sensitive features due to oxidation of Ni^{2+} sites.

DOI: 10.1021/ja511559d
J. Am. Chem. Soc. 2015, 137, 1305−1313

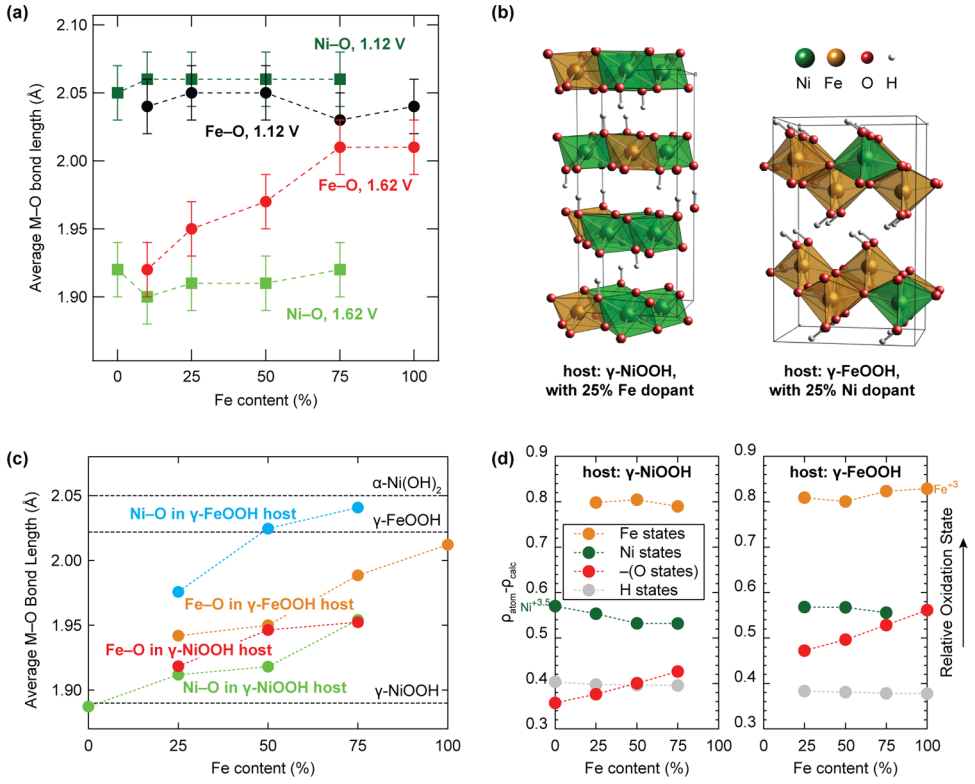

Figure 3. Identification of the most likely structural motif for mixed Ni,Fe catalysts by comparison of experimentally obtained metal−oxygen bond lengths with optimized theoretical model structures. (a) Bond lengths extracted from HERFD XAS measurements at 1.12 and 1.62 V, plotted as a function of Fe content. (b) Examples of unit cells for Fe-substituted γ-NiOOH and Ni-substituted γ-FeOOH model structures. (c) Theoretically predicted bond lengths, corrected by a factor of 0.97 for comparison with experimental data. The dashed lines represent experimental bond lengths from literature (see Supporting Information S12). (d) Löwdin charges in Fe-substituted γ-NiOOH and Ni-substituted γ-FeOOH model structures, plotted as a function of Fe content. All dashed lines are guides to the eye.

when the potential is increased from 1.12 to 1.52 V; the features of the oxidized component then approach saturation with further potential increase. A more detailed analysis (Supporting Information S10) confirms that the observed redox transition is indeed that between α-Ni(OH)$_2$ and γ-NiOOH; the presence of β-Ni(OH)$_2$ or β-NiOOH can be ruled out. Both the Fe and Ni K-edge spectra exhibit shifts of the structure-sensitive EXAFS dips and peaks to higher energy, indicating significant bond contraction. Using the "bond length with a ruler" relationship $(E_{peak} - E_0)d^2 = \text{const.}$,[58,59] which is equivalent to an EXAFS analysis with a strongly reduced number of independent fitting parameters (see Supporting Information S11), we estimate a bond length contraction of (7 ± 1)% at both Fe and Ni sites. This result was further refined with EXAFS measurements over a much larger energy range for a Fe/Ni (25:75) sample in the fully reduced and fully oxidized state. EXAFS confirms that the Fe−O and Ni−O bond lengths contract from 2.01 and 2.06 Å at 1.12 V to 1.90 and 1.89 Å at 1.92 V, respectively (Figure 2c, Table 1), and the result in Figure 2c was not affected by the catalyst preparation method (sputter deposition followed by electrochemical oxidation, see Supporting Information S2 for results with an electrodeposited film). A strong correlation was found not only between Fe−O and Ni−O bond lengths but also between nearest metal−metal distances, indicating that Fe substitutes for Ni in both α-Ni(OH)$_2$ and γ-NiOOH. Moreover, the identical appearance in both Fe and Ni K-edge EXAFS of a peak at approximately twice the nearest Ni−Ni and Fe−Ni distance, predominantly from multiple-scattering in collinear Fe−Ni−Ni, Ni−Fe−Ni and

Table 1. EXAFS Fit Results for Catalyst Containing 75% Ni/25% Fe[a]

	Ni K-edge		Fe K-edge	
E = 1.12 V	Ni−O	Ni−Ni	Fe−O	Fe−Ni
CN	6.5 ± 0.6	5.5 ± 0.6	6.5 ± 0.6	5.9 ± 0.7
distance (Å)	2.06 ± 0.01	3.10 ± 0.01	2.01 ± 0.01	3.10 ± 0.01
σ^2 (Å^{-2})	0.005	0.005	0.005	0.007
k-range (Å^{-1})	2.0−11.7		2.0−11.5	
r range (Å)	0.6−3.4		0.6−3.5	
R factor	0.05		0.015	
E_0 (eV)	−1.6 ± 1.9		−1.6 ± 1.8	
	Ni K-edge		Fe K-edge	
E = 1.62 V	Ni−O	Ni−Ni	Fe−O	Fe−Ni
CN	6.1 ± 0.9	5.4 ± 0.7	5.4 ± 0.9	5.2 ± 0.7
distance (Å)	1.89 ± 0.02	2.82 ± 0.01	1.90 ± 0.02	2.84 ± 0.02
σ^2 (Å^{-2})	0.005	0.005	0.005	0.005
k-range (Å^{-1})	2.0 to 11.7		2.0−11.5	
r range (Å)	0.6−3.0		0.6−3.0	
R factor	0.094		0.028	
E_0 (eV)	−2.4 ± 2.4		−4.8 ± 2.9	

[a]This catalyst sample was made by sputter-deposition followed by electrochemical oxidation. Values shown without error bars were not allowed to vary in the fit. S_0^2 was fixed at 0.90.

DOI: 10.1021/ja511559d
J. Am. Chem. Soc. 2015, 137, 1305−1313

Ni−Ni−Ni arrangements, clearly shows that Fe is not intercalated between the hexagonal [NiO_2] sheets but instead substitutes for Ni within the sheets.

Further examination of the HERFD XAS reveals important information about the oxidation states of Fe and Ni in Fe-substituted α-$Ni(OH)_2$ and γ-NiOOH. Contracted bond distances are commonly associated with an increased oxidation state, and such oxidation state increase can be clearly seen in the Ni K-edge spectra where the pre-edge centroid and the photoionization threshold both shift to significantly higher energy. In contrast, an intriguing discrepancy can be seen in the Fe K-edge spectra. Comparison of the short Fe−O distance of (1.90 ± 0.01) Å at 1.62 V with bond lengths for different Fe oxides reported in the literature (Supporting Information S12) suggests that all Fe sites should have increased their oxidation state from +3 to +4. However, if such a significant oxidation state increase occurred at all Fe sites, we would have expected more noticeable shifts to higher energies of both the pre-edge centroid as well as the photoionization threshold. In XANES spectra of the $La_{1-x}Sr_xFeO_4$ series,[60−62] in which Fe has the formal oxidation states of +3 and +4 for the end members $x = 0$ and $x = 1$, respectively, the pre-edge centroid shifts by ∼0.7 eV and the multiplet structure changes significantly from the characteristic doublet for Fe^{3+} in octahedral coordination to a much more intense single peak for Fe^{4+}. Main edge shifts up to 1.26 eV have been reported in the same series. In the present study, such changes are much less pronounced; furthermore, two additional characteristics of Fe^{4+} in $SrFeO_4$ due to increased Fe−O covalency, i.e., a ligand-to-metal charge transfer (LMCT) shakedown feature near the main edge and a strong decrease of the white line intensity, are not observed for Fe-containing γ-NiOOH. Subtle changes in the pre-edge region might suggest a small fraction of Fe^{4+} sites, but this cannot account for the bond contraction, which clearly affects all Fe sites and is imposed through the edge-sharing of [FeO_6] and surrounding [NiO_6] octahedra.

For all other Fe/Ni ratios, average Ni−O and Fe−O bond lengths at different potentials can be obtained by applying either the same relation [$(E_{peak} - E_0)d^2$ = const.] as above, or linear combination fits using the two spectra of the Ni/Fe (75:25) sample at 1.12 and 1.92 V as components, which sufficiently reproduce all other spectra (Supporting Information S10). The results are shown in Figure 3a for two potentials, the resting state at 1.12 V as well as OER operating conditions at 1.62 V. Irrespective of the presence and concentration of Fe, the Ni−O bond lengths correspond to α-$Ni(OH)_2$ and γ-NiOOH at low and high potentials, respectively. Conversely, the average Fe−O bond length completely follows the Ni−O bond contraction only at low Fe content (10 and 25%). With increasing Fe content, the Fe−O distance at 1.62 V gradually increases toward that of pure γ-FeOOH. We propose that two different Fe^{3+} species are present, i.e., Fe^{3+} dopants in α-$Ni(OH)_2$/γ-NiOOH and Fe^{3+} sites within a separate γ-FeOOH phase. While a single Ni/Fe phase exists at low Fe content, FeOOH increasingly contributes to the Fe K-edge spectra with increasing overall Fe content, due to limited solubility of Fe^{3+} in α-$Ni(OH)_2$. A more recent study of Fe uptake into $Ni(OH)_2$ from Fe-containing KOH solution indicates such a solubility limit near 25% Fe.[63]

Since we do not observe Ni−O bond expansion even at 75% Fe content, we estimate based on experimental uncertainty in the Ni−O bond distance, that Ni doping into γ-FeOOH, if any, does not exceed 3%. The proposed interpretation is illustrated schematically in Figure 1 (top). The different solubility limits for Fe in $Ni(OH)_2$/NiOOH and Ni in FeOOH could be attributed to differences in the capability of the host structures to compensate the charge difference between Ni^{2+} and Fe^{3+} that are present at low potential and, presumably, during catalyst electrodeposition. The α-$Ni(OH)_2$ structure contains intercalated H_2O between the hexagonal [NiO_2] sheets, and can accommodate electrolyte anions (e.g., SO_4^{2-}). In the resulting charge-neutral $Ni(II)_{1-x}Fe(III)_x(OH)_2(SO_4)_{x/2}(H_2O)_y$ layered double hydroxide structure,[31] Fe uptake will be enabled by closely matching Fe^{3+}−O and Ni^{2+}−O distances but limited by steric hindrance and repulsion between partially hydrated anions. Conversely, there is no obvious pathway for the γ-FeOOH structure to allow intercalation of cations (e.g., K^+) or protonation of O or OH ligands without a significant distortion of linkages between [MO_6] octahedra. Correspondingly, the absence of intercalation in β-$Ni(OH)_2$ could explain why the presence of Fe^{3+} appears to prevent the transformation ("aging") of α-$Ni(OH)_2$ into β-$Ni(OH)_2$.[21]

DFT+U calculations were carried out in order to further understand the effects of Fe substitution into γ-NiOOH and Ni substitution into γ-FeOOH (see Supporting Information S3−S5 for details). The model structures shown in Figure 3b capture the known oxidation states and local binding environment of metal sites but neglect the role of intercalated species that have not been well characterized experimentally (Supporting Information S3). The DFT+U method offers an improved description of correlated transition metal oxides over commonly used DFT at minimal additional cost,[64,65] which makes this approach optimal for materials screening and optimization; however some deficiencies of DFT remain.[66] A comparison of theoretically predicted metal−oxygen bond lengths (Figure 3c and Supporting Information S4) with the experimental values from our measurements (Figure 3a) and literature (Supporting Information S12) supports our hypothesis that only Fe-doped γ-NiOOH and pure FeOOH, but very little, if any, Ni-doped γ-FeOOH, exist under OER conditions.

Löwdin charges of Ni, Fe, O, and H relative to the free atoms were obtained from the DFT+U results in order to provide a measure of the apparent oxidation states of these elements. Figure 3d shows that the Löwdin charges for both Fe and Ni remain approximately constant for all model structures investigated. This finding agrees with our experimental observation that Fe and Ni oxidation states under OER conditions are +3 and +3.6 (average), respectively, independent of the Ni/Fe ratio. We also note that the Löwdin charge for Fe is significantly higher than for Ni despite the opposite order of formal oxidation states of both cations. This difference reflects the nature of the metal−oxygen bonds, which are more ionic and less covalent for Fe than for Ni. Likewise, the linear increase in negative charge on the O atoms with increasing Fe content is attributable to the replacement of the more covalent Ni−O bonds with the more ionic Fe−O bonds.

In summary, our operando HERFD-XAS data demonstrate that for Fe contents lower than ∼25%, Fe^{3+} cations substitute for Ni^{3+} cations into the lattice of γ-NiOOH. This modification has no effect on the oxidation state of the Ni cations. We observe, however, that the Fe−O bond distance in $Ni_{1-x}Fe_xOOH$ is 6% shorter than that found in γ-FeOOH, and, for small Fe content up to 25%, is almost identical to that of Ni−O. With increasing Fe content the Ni−O bond distance remains nearly constant, whereas the average Fe−O bond distance increases steadily, becoming comparable to that for γ-

DOI: 10.1021/ja511559d
J. Am. Chem. Soc. 2015, 137, 1305−1313

FeOOH at Fe contents above 75%. DFT+U calculations confirm that a Fe−O bond distance similar to that for Ni−O should be observed when Fe^{3+} cations substitute for Ni^{3+} cations in γ-$Ni_{1-x}Fe_xOOH$. The absence of any experimental evidence for Ni−O bond expansion in materials prepared with Fe contents above 50% suggests that for Fe contents in excess of ∼25%, a γ-FeOOH phase is nucleated that does not contain a large amount of Ni in it.

We note that our conclusions concerning the oxidation state of Fe and the Fe−O bond distance for Fe cations present in Fe-substituted γ-NiOOH differ from those reported earlier.[30,32] Previous XANES and EXAFS studies of Fe-doped NiOOH yielded contradictory results regarding the local structure and oxidation state of Fe. Kim et al. reported that Fe in γ-NiOOH remains as Fe^{3+};[30] the Fe−O bond length was found to be 1.92 Å independent of applied potential and was stated to be "essentially identical" to that in β-FeOOH and γ-FeOOH, although both sources cited for this value actually reported average bond lengths of 2.05 and 2.03 Å, respectively.[67,68] By contrast, Balasubramanian et al. reported oxidation of Fe^{3+} to Fe^{4+} and an Fe−O distance of 1.94 Å.[32] We suggest that in both refs 30 and 32, Ni oxidation could have been incomplete, since measurements under OER conditions were not carried out. We note further that HERFD XAS measurements and supporting DFT+U calculations rule out the formation of significant concentrations of Fe^{4+} cations in Fe-doped γ-NiOOH. It is important to note that energy shifts of the $1s \rightarrow 4p$ resonance, reported by Balasubramanian et al. as an indication for Fe^{4+} formation, can arise not only from oxidation state changes, which shift the 1*s* core level, but also energy shifts in the 4*p* unoccupied pDOS due to altered bond lengths. In the present case, the energy shift of ∼1 eV can be explained with the Fe−O bond contraction alone and is too small to account for an additional core level shift, as shown in our more detailed analysis given in Figure S5.

Our interpretation of the changes in the structure of γ-$Ni_{1-x}Fe_xOOH$ with increasing Fe content suggests that the observed changes in OER activity shown in Figure 1 can be explained in the following manner. Addition of Fe to γ-NiOOH initially increases the OER activity to due to the substitution of Fe^{3+} cations in the framework of γ-NiOOH. A plateau in activity is reached at ∼25% Fe content, beyond which further increases in the catalyst content of Fe results in the growth of catalytically inactive γ-FeOOH, with the net effect that the catalyst activity declines as the fraction of the less active to the more active catalyst increases.

Not addressed to this point, though, is why the substitution of Fe^{3+} into the lattice of γ-NiOOH increases the OER activity of the catalyst. Two options exist: one is that the substituted Fe^{3+} sites become more active when hosted in the lattice of γ-NiOOH due to a change in their electronic environment, and the other is that the activity of Ni^{3+} sites increases as a consequence of their electronic properties being altered by the substitution of Fe^{3+} cations into the γ-NiOOH lattice. Another question to ask is whether the small amount of Ni^{3+} that can substitute into γ-FeOOH has an effect on the OER activity of this phase, and if so how so. As we will next show, both sets of questions can be addressed by DFT+U calculations of the overpotential for the OER. This will be done using standard procedures, which have been demonstrated to give solid basis for interpreting the relationship between catalyst composition and OER overpotential.[28,69−71]

In acidic conditions, the OER is taken to occur via four elementary steps:

$$H_2O + * \rightarrow OH^* + e^- + H^+ \quad (1)$$

$$OH^* \rightarrow O^* + e^- + H^+ \quad (2)$$

$$O^* + H_2O \rightarrow OOH^* + e^- + H^+ \quad (3)$$

$$OOH^* \rightarrow O_2 + e^- + H^+ \quad (4)$$

with * indicating an oxygen vacancy site at the surface. The computational hydrogen electrode[69] was used to express the chemical potentials of protons and electrons at any given pH and applied potential *U*. As a result, the theoretical overpotential η obtained from Gibbs free energy differences ΔG_i (i = 1, ..., 4) at each step as

$$\eta = \max[\Delta G_1, \Delta G_2, \Delta G_3, \Delta G_4]/e - 1.23[\mathrm{V}] \quad (5)$$

is independent of pH and is therefore applicable to alkaline conditions. Further details of the computational methodology are given in the Supporting Information S5.

Figure 4 compares predicted overpotentials for the OER occurring at Ni and Fe surface sites in pure and doped γ-NiOOH and γ-FeOOH. The choice of surface terminations for γ-NiOOH was influenced by previous works for structurally similar CoOOH,[72] were it was found that the natural (0001) facet leads to low OER activity, while higher index surfaces such as $(01\bar{1}2)$ or $(01\bar{1}4)$, which contain under-coordinated metal sites similar to step or edge have more active sites. The results can be rationalized in terms of the overall affinity of surface sites for adsorbed intermediates and the relative stability of O* with respect to OH* and OOH*. Generally much weaker adsorption is found for the on-top position of a single 5-fold coordinated metal atom than for the bridge site between two 5-fold coordinated metal atoms, and Fe sites have significantly higher OH affinity than Ni sites. While the difference between adsorption energies of OH* and OOH* is nearly constant, $\Delta E_{OOH} = 0.8\Delta E_{OH} + 3.3$ eV, the O* binding energy increases as a function of ΔE_{OH} (see Figure S14). Under the optimum condition $\Delta E_O - \Delta E_{OH} = 0.5(\Delta E_{OOH} - \Delta E_{OH})$,[71] η reaches a minimum value of 0.4 V. In the absence of doping, all OER intermediates adsorb too strongly on pure γ-FeOOH and too weakly on pure γ-NiOOH. The calculated overpotentials for Fe-free γ-NiOOH are larger than that for pure γ-FeOOH, in very good agreement with the results presented in Figure 1.

Compared to pure γ-FeOOH, Fe sites surrounded by Ni next-nearest neighbors in either γ-NiOOH or γ-FeOOH host structures exhibit decreased affinity for OER intermediates, resulting in a shift in their binding energies toward optimal values. The origin of these trends can be rationalized based on the results in Figure 3d, which show that $Ni^{3+/4+}$ cations, due to their higher electron affinity compared to Fe^{3+}, withdraw electron density from oxygen sites. During OER, the formation of HO* and O* requires an oxidation state increase at the active Fe site, which becomes evident, for example, in the notably short bond distance of 1.62 Å between O* and a highly charged Fe site in Fe-doped γ-NiOOH$(01\bar{1}2)$ (Figure 4a). The oxidation of the Fe surface site will be less favorable energetically in γ-NiOOH than in γ-FeOOH, because neighboring Ni sites induce lower negative charge density on adsorbed O and OH. We propose that this effect is mostly determined by the local arrangement of neighboring Fe and Ni sites. Computational results for structurally similar Ni-doped

DOI: 10.1021/ja511559d
J. Am. Chem. Soc. 2015, 137, 1305−1313

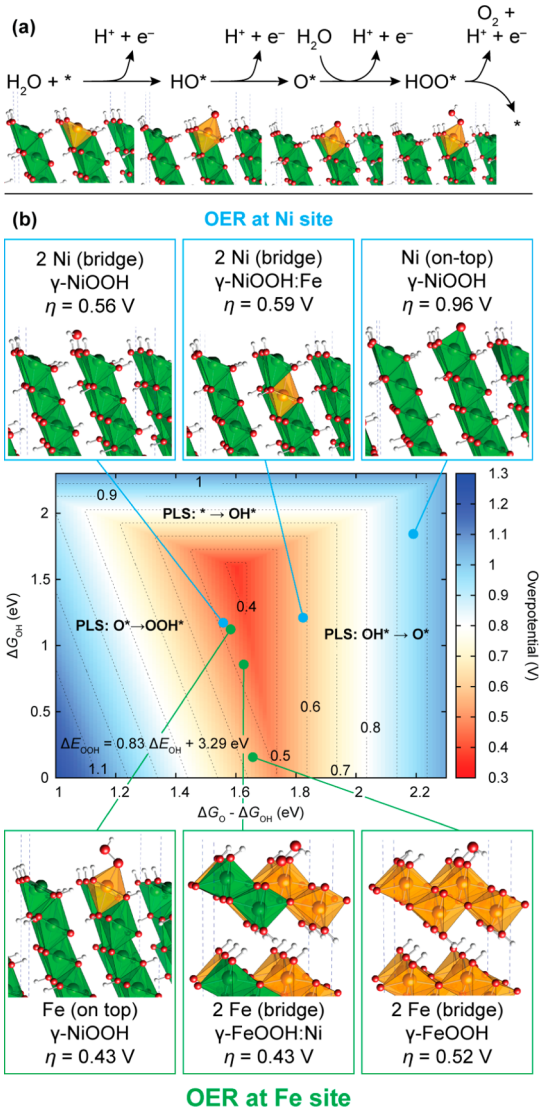

Figure 4. Theoretical OER overpotentials at Ni and Fe surface sites in pure and doped γ-NiOOH and γ-FeOOH model structures. (a) Proposed OER pathway with intermediates HO*, O* and HOO*, illustrated using the example of the on-top site at a substituted Fe surface atom in γ-NiOOH(01$\bar{1}$2). The binding energies of these species are used to estimate the OER overpotential. (b) OER activity volcano showing the overpotential as a function of Gibbs free energies of the reaction intermediates. Computed overpotentials are shown for the OER at Ni–Ni bridge and Fe on-top sites located in pure γ-NiOOH(01$\bar{1}$2) and in γ-NiOOH(01$\bar{1}$2) with Fe surface and subsurface doping, at a Ni on-top site in pure γ-NiOOH(01$\bar{1}$2), and at Fe–Fe bridge sites in pure and Ni-doped γ-FeOOH(010) (25% Ni in bulk unit cell). All corresponding model structures are shown with the intermediate whose formation is the potential limiting step (PLS) (HOO* in all cases except for the on-top Ni site in γ-NiOOH(01$\bar{1}$2) and γ-NiOOH(01$\bar{1}$2) with subsurface Fe, where formation of O* determines the overpotential).

hematite indicate the same mechanism for the catalytic enhancement, further supporting our hypothesis.[28]

Further calculations comparing the overpotentials for the OER occurring over Ni or Fe sites confirm that Fe rather than Ni constitutes the active site for the OER at mixed Fe–Ni oxyhydroxides. Subsurface Fe sites in γ-NiOOH (Figure 4b) increase the OER overpotential at Ni surface sites because the already too weak oxygen affinity of Ni further decreases. This finding is consistent with the experimentally observed shift of the α-Ni(OH)$_2$/γ-NiOOH redox potential to higher values with increasing Fe content.[23]

It is important at this stage to compare and contrast our theoretical results with those of Li and Selloni,[26] who report DFT+U calculations of the OER overpotentials for β- and γ-NiOOH and for Fe substituted into the surface of both NiOOH phases. While there are substantial differences in the catalyst structure, the sequence of steps leading to the oxidation of water, and the computational approach used in this study and the present one, both studies agree that the OER overpotential for Fe-doped γ-NiOOH is lower than that for pure γ-NiOOH. Thus, Li and Selloni find that η = 0.48 V for Fe-doped γ-NiOOH and η = 0.52 V for pure γ-NiOOH, whereas we find that η = 0.43 V for Fe-doped γ-NiOOH and η = 0.56 V for pure γ-NiOOH. Li and Selloni also predict that an even lower overpotential for the OER can be achieved on Fe-doped β-NiOOH (η = 0.26 V) and that the overpotential for pure β-NiOOH should be lower than that for γ-NiOOH (η = 0.46 for β-NiOOH versus η = 0.52 for γ-NiOOH). While we note that these are interesting findings, we did not observe any evidence for the β phase of NiOOH in our experiments, and recent work by Trotochaud et al. indicates that the presence of Fe in the active phase of Ni–Fe oxides inhibits the formation of this phase.[21]

It is significant to note that the conclusions regarding the influence of Fe on the overpotential for the OER deduced from the present work differ from those that would have been made in the absence of this effort. Prior to this study and based on the observation that addition of Fe to NiOOH results in an increase of the redox potential for the equilibrium between α-Ni(OH)$_2$ and γ-NiOOH, we had speculated that the altered relative stability of Ni^{2+}, Ni^{3+} and Ni^{4+} sites could be the dominant factor affecting the activation barriers for the OER. This reasoning was based on the assumption that an OER-active metal site would undergo oxidation state changes during the elementary steps of the OER. Furthermore, measurements of the charge required to reduce Fe–Ni OER catalysts from their operating state to α-Ni(OH)$_2$ seemed to indicate a lower average Ni oxidation state in Fe-doped NiOOH compared to pure NiOOH.[23] On the basis of these observations, "chemical intuition" suggested that the most active site in (Fe,Ni)OOH would be a Ni cation. In contrast to previous coulometric analysis,[23] our XAS results indicate that under OER conditions Ni sites have the same average oxidation state, independent of Fe content. This finding does not contradict the anodic shift of the α-Ni(OH)$_2$/γ-NiOOH redox potential but merely indicates that the redox potential, although it increases, does not exceed the onset potential for the OER. What we must conclude, therefore, is that the local electronic structure of Ni cations in Fe-doped NiOOH during OER cannot be distinguished by XAS from that in pure NiOOH. Nevertheless, XAS does reveal a strong influence of the Ni host structure on the local structure at Fe cations.

While it might still be argued that XAS only captures bulk-averaged electronic structure information and therefore may not be representative of minority Ni species at the surface, the DFT+U results reveal unambiguously how the reactivity of surface Ni and Fe sites is altered. We conclude that "chemical intuition" was actually correct insofar as Ni surface sites were assumed to bind OER intermediates more weakly in γ-Fe$_x$Ni$_{1-x}$OOH than in γ-NiOOH; however, the calculation also reveal that the resulting adsorption at Ni surface sites is

DOI: 10.1021/ja511559d
J. Am. Chem. Soc. 2015, 137, 1305–1313

much weaker than what is required for an "optimal" catalyst and therefore cannot account for the significant reduction in the OER overpotential observed experimentally. By contrast, nearly optimal adsorption energies are achieved at Fe sites in $Fe_xNi_{1-x}OOH$.

CONCLUSIONS

In situ HERFD XAS data were acquired in order to establish the local electronic environment of Ni and Fe cations in Fe-doped NiO_x catalysts used for the OER. Changes in the oxidation and metal-to-oxygen bond distance were observed with increasing applied potential. At potentials well below the onset of the OER, the Ni is present as α-$Ni(OH)_2$ in the absence of Fe, and as $Ni(II)_{1-x}Fe(III)_x(OH)_2(SO_4)_{x/2}(H_2O)_y$, a layered double hydroxide structure, in the presence of Fe. While Ni is present in the double hydroxide as Ni^{2+}, Fe is present as Fe^{3+}, in both cases independent of the amount of Fe added. As the potential is raised, but still below that for the onset of the OER, the Ni cations undergo oxidation to Ni^{3+}; however, the Fe cations remain as Fe^{3+}. For Fe levels below about 25%, the oxidized catalyst can be described as γ-$Ni_{1-x}Fe_xOOH$, reflecting the substitution of Ni by Fe cations. What is notable in this material is that the Ni−O and Fe−O bond distances are very similar and both are comparable to the Ni−O bond distance in γ-NiOOH. It is also notable that the Fe−O bond distance is ∼6% shorter than that in γ-FeOOH. As the Fe level rises above 25%, the XAS data suggest that a γ-FeOOH phase nucleates, which contains either no or <3% Ni. The conclusions drawn about the effects of Fe on the composition and structure of the oxidized catalyst are supported by DFT+U calculations. Insights into the cause for the rapid increase in OER activity of $Ni_{1-x}Fe_xOOH$ with increasing Fe content can also be obtained from DFT+U calculations of the OER overpotential. What is found is that Fe^{3+} cations in γ-$Ni_{1-x}Fe_xOOH$ exhibit a significantly lower overpotential than do Ni^{3+} cations in either γ-$Ni_{1-x}Fe_xOOH$ or γ-NiOOH. Such calculations and those by others[28] also reveal that, in addition to γ-$Ni_{1-x}Fe_xOOH$, a variety of other materials with edge-sharing $[FeO_6]$ and $[NiO_6]$ octahedra, such as Ni-doped γ-FeOOH and Ni-doped hematite[28] are predicted to have superior OER activity at Fe sites.

ASSOCIATED CONTENT

Supporting Information

Catalyst preparation, additional EXAFS measurements on electrodeposited catalyst layers, choice of model (Ni,Fe)OOH structures for DFT+U, optimized bulk structures and their density of states, calculation of OER overpotentials, OER activity measurements, purification of KOH electrolyte, complete set of operando HERFD XAS measurements, HERFD XAS of Fe and Ni reference compounds, linear combination fitting of operando HERFD XAS, bond contraction from HERFD XAS, comparison of structure information from HERFD XAS and EXAFS. This material is available free of charge via the Internet at http://pubs.acs.org.

AUTHOR INFORMATION

Corresponding Authors

dfriebel@slac.stanford.edu
alexbell@berkeley.edu

Author Contributions

[¶]D.F., M.W.L., and M.B. contributed equally.

Notes

The authors declare no competing financial interest.

ACKNOWLEDGMENTS

This material is based upon work performed by the Joint Center for Artificial Photosynthesis, a DOE Energy Innovation Hub, supported through the Office of Science of the U.S. Department of Energy under Award Number DE-SC0004993. This research was partly carried out at the Stanford Synchrotron Radiation Lightsource, a National User Facility operated by Stanford University on behalf of the U.S. Department of Energy, Office of Basic Energy Sciences. We thank Lena Trotochaud, Harri Ali-Löytti and Lin Li for their assistance with data collection. We are grateful to Uwe Bergmann, Thomas Bligaard, Aleksandra Vojvodic and Lena Trotochaud for helpful discussions. We thank Tyler Matthews for assistance with sample preparation. M.W.L. was partially supported by the University of California President's Postdoctoral Fellowship. K.E.S. gratefully acknowledges the Ernest-Solvay-Stiftung for financial support. This research employed NERSC computational resources under DOE Contract No. DE-AC02-05CH11231.

REFERENCES

(1) Walter, M. G.; Warren, E. L.; McKone, J. R.; Boettcher, S. W.; Mi, Q.; Santori, E. A.; Lewis, N. S. *Chem. Rev.* **2010**, *110*, 6446.
(2) Trasatti, S. *Electrochim. Acta* **1984**, *29*, 1503.
(3) Lee, S. W.; Carlton, C.; Risch, M.; Surendranath, Y.; Chen, S.; Furutsuki, S.; Yamada, A.; Nocera, D. G.; Shao-Horn, Y. *J. Am. Chem. Soc.* **2012**, *134*, 16959.
(4) Risch, M.; Grimaud, A.; May, K. J.; Stoerzinger, K. A.; Chen, T. J.; Mansour, A. N.; Shao-Horn, Y. *J. Phys. Chem. C* **2013**, *117*, 8628.
(5) Suntivich, J.; May, K. J.; Gasteiger, H. A.; Goodenough, J. B.; Shao-Horn, Y. *Science* **2011**, *334*, 1383.
(6) Subbaraman, R.; Tripkovic, D.; Chang, K.-C.; Strmcnik, D.; Paulikas, A. P.; Hirunsit, P.; Chan, M.; Greeley, J.; Stamenkovic, V.; Markovic, N. M. *Nat. Mater.* **2012**, *11*, 550.
(7) McCrory, C. C. L.; Jung, S.; Peters, J. C.; Jaramillo, T. F. *J. Am. Chem. Soc.* **2013**, *135*, 16977.
(8) Kanan, M. W.; Nocera, D. G. *Science* **2008**, *321*, 1072.
(9) Bediako, D. K.; Lassalle-Kaiser, B.; Surendranath, Y.; Yano, J.; Yachandra, V. K.; Nocera, D. G. *J. Am. Chem. Soc.* **2012**, *134*, 6801.
(10) Khaselev, O.; Turner, J. A. *Science* **1998**, *280*, 425.
(11) Jin, J.; Walczak, K.; Singh, M. R.; Karp, C.; Lewis, N. S.; Xiang, C. *Energy Environ. Sci.* **2014**, *7*, 3371.
(12) Hu, S.; Xiang, C.; Haussener, S.; Berger, A. D.; Lewis, N. S. *Energy Environ. Sci.* **2013**, *6*, 2984.
(13) Gregoire, J. M.; Xiang, C.; Mitrovic, S.; Liu, X.; Marcin, M.; Cornell, E. W.; Fan, J.; Jin, J. *J. Electrochem. Soc.* **2013**, *160*, F337.
(14) Trotochaud, L.; Mills, T. J.; Boettcher, S. W. *J. Phys. Chem. Lett.* **2013**, *4*, 931.
(15) Młynarek, G.; Paszkiewicz, M.; Radniecka, A. *J. Appl. Electrochem.* **1984**, *14*, 145.
(16) Corrigan, D. A. *J. Electrochem. Soc.* **1987**, *134*, 377.
(17) Miller, E. L.; Rocheleau, R. E. *J. Electrochem. Soc.* **1997**, *144*, 3072.
(18) Li, X.; Walsh, F. C.; Pletcher, D. *Phys. Chem. Chem. Phys.* **2010**, *13*, 1162.
(19) Landon, J.; Demeter, E.; İnoğlu, N.; Keturakis, C.; Wachs, I. E.; Vasić, R.; Frenkel, A. I.; Kitchin, J. R. *ACS Catal.* **2012**, *2*, 1793.
(20) Trotochaud, L.; Ranney, J. K.; Williams, K. N.; Boettcher, S. W. *J. Am. Chem. Soc.* **2012**, *134*, 17253.
(21) Trotochaud, L.; Young, S. L.; Ranney, J. K.; Boettcher, S. W. *J. Am. Chem. Soc.* **2014**, *136*, 6744.
(22) Gong, M.; Li, Y.; Wang, H.; Liang, Y.; Wu, J. Z.; Zhou, J.; Wang, J.; Regier, T.; Wei, F.; Dai, H. *J. Am. Chem. Soc.* **2013**, *135*, 8452.

DOI: 10.1021/ja511559d
J. Am. Chem. Soc. 2015, 137, 1305−1313

(23) Louie, M. W.; Bell, A. T. *J. Am. Chem. Soc.* **2013**, *135*, 12329.
(24) Smith, R. D. L.; Prévot, M. S.; Fagan, R. D.; Trudel, S.; Berlinguette, C. P. *J. Am. Chem. Soc.* **2013**, *135*, 11580.
(25) Smith, R. D. L.; Prévot, M. S.; Fagan, R. D.; Zhang, Z.; Sedach, P. A.; Siu, M. K. J.; Trudel, S.; Berlinguette, C. P. *Science* **2013**, *340*, 60.
(26) Li, Y.-F.; Selloni, A. *ACS Catal.* **2014**, 1148.
(27) Gao, M.; Sheng, W.; Zhuang, Z.; Fang, Q.; Gu, S.; Jiang, J.; Yan, Y. *J. Am. Chem. Soc.* **2014**, *136*, 7077.
(28) Liao, P.; Keith, J. A.; Carter, E. A. *J. Am. Chem. Soc.* **2012**, *134*, 13296.
(29) Corrigan, D. A.; Conell, R. S.; Fierro, C. A.; Scherson, D. A. *J. Phys. Chem.* **1987**, *91*, 5009.
(30) Kim, S.; Tryk, D. A.; Antonio, M. R.; Carr, R.; Scherson, D. *J. Phys. Chem.* **1994**, *98*, 10269.
(31) Guerlou-Demourgues, L.; Fournès, L.; Delmas, C. *J. Electrochem. Soc.* **1996**, *143*, 3083.
(32) Balasubramanian, M.; Melendres, C. A.; Mini, S. *J. Phys. Chem. B* **2000**, *104*, 4300.
(33) Eisenberger, P.; Platzman, P. M.; Winick, H. *Phys. Rev. Lett.* **1976**, *36*, 623.
(34) Hämäläinen, K.; Siddons, D. P.; Hastings, J. B.; Berman, L. E. *Phys. Rev. Lett.* **1991**, *67*, 2850.
(35) Heijboer, W. M.; Glatzel, P.; Sawant, K. R.; Lobo, R. F.; Bergmann, U.; Barrea, R. A.; Koningsberger, D. C.; Weckhuysen, B. M.; de Groot, F. M. F. *J. Phys. Chem. B* **2004**, *108*, 10002.
(36) Friebel, D.; Bajdich, M.; Yeo, B. S.; Louie, M. W.; Miller, D. J.; Casalongue, H. S.; Mbuga, F.; Weng, T.-C.; Nordlund, D.; Sokaras, D.; Alonso-Mori, R.; Bell, A. T.; Nilsson, A. *Phys. Chem. Chem. Phys.* **2013**, *15*, 17460.
(37) Sokaras, D.; Weng, T.-C.; Nordlund, D.; Alonso-Mori, R.; Velikov, P.; Wenger, D.; Garachtchenko, A.; George, M.; Borzenets, V.; Johnson, B.; Rabedeau, T.; Bergmann, U. *Rev. Sci. Instrum.* **2013**, *84*, 053102.
(38) Webb, S. M. *Phys. Scr.* **2005**, *T115*, 1011.
(39) Newville, M. *J. Synchrotron Radiat.* **2001**, *8*, 322.
(40) Ravel, B.; Newville, M. *J. Synchrotron Radiat.* **2005**, *12*, 537.
(41) Zabinsky, S. I.; Rehr, J. J.; Ankudinov, A.; Albers, R. C.; Eller, M. J. *Phys. Rev. B: Condens. Matter Mater. Phys.* **1995**, *52*, 2995.
(42) Christensen, H.; Christensen, A. *Acta Chem. Scand., Ser. A* **1978**, *32*, 87.
(43) Bartl, H.; Bode, H.; Sterr, G.; Witte, J. *Electrochim. Acta* **1971**, *16*, 615.
(44) Anisimov, V. I.; Aryasetiawan, F.; Lichtenstein, A. I. *J. Phys.: Condens. Matter* **1997**, *9*, 767.
(45) Anisimov, V. I.; Zaanen, J.; Andersen, O. K. *Phys. Rev. B: Condens. Matter Mater. Phys.* **1991**, *44*, 943.
(46) Bacq, O. L.; Pasturel, A.; Bengone, O. *Phys. Rev. B: Condens. Matter Mater. Phys.* **2004**, *69*, 245107.
(47) Hammer, B.; Hansen, L. B.; Nørskov, J. K. *Phys. Rev. B: Condens. Matter Mater. Phys.* **1999**, *59*, 7413.
(48) Dudarev, S. L.; Botton, G. A.; Savrasov, S. Y.; Humphreys, C. J.; Sutton, A. P. *Phys. Rev. B: Condens. Matter Mater. Phys.* **1998**, *57*, 1505.
(49) Cococcioni, M.; de Gironcoli, S. *Phys. Rev. B: Condens. Matter Mater. Phys.* **2005**, *71*, 035105.
(50) Vanderbilt, D. *Phys. Rev. B: Condens. Matter Mater. Phys.* **1990**, *41*, 7892.
(51) Giannozzi, P.; Baroni, S.; Bonini, N.; Calandra, M.; Car, R.; Cavazzoni, C.; Ceresoli, D.; Chiarotti, G. L.; Cococcioni, M.; Dabo, I.; Dal Corso, A.; de Gironcoli, S.; Fabris, S.; Fratesi, G.; Gebauer, R.; Gerstmann, U.; Gougoussis, C.; Kokalj, A.; Lazzeri, M.; Martin-Samos, L.; Marzari, N.; Mauri, F.; Mazzarello, R.; Paolini, S.; Pasquarello, A.; Paulatto, L.; Sbraccia, C.; Scandolo, S.; Sclauzero, G.; Seitsonen, A. P.; Smogunov, A.; Umari, P.; Wentzcovitch, R. M. *J. Phys.: Condens. Matter* **2009**, *21*, 395502.
(52) Westre, T. E.; Kennepohl, P.; DeWitt, J. G.; Hedman, B.; Hodgson, K. O.; Solomon, E. I. *J. Am. Chem. Soc.* **1997**, *119*, 6297.
(53) Capehart, T. W.; Corrigan, D. A.; Conell, R. S.; Pandya, K. I.; Hoffman, R. W. *Appl. Phys. Lett.* **1991**, *58*, 865.
(54) Mansour, A. N.; Melendres, C. A. *Phys. B* **1995**, *208*−*209*, 583.
(55) Hu, Y.; Bae, I. T.; Mo, Y.; Scherson, D. A.; Antonio, M. R. *Can. J. Chem.* **1997**, *75*, 1721.
(56) Morishita, M.; Ochiai, S.; Kakeya, T.; Ozaki, T.; Kawabe, Y.; Watada, M.; Tanase, S.; Sakai, T. *Electrochemistry* **2008**, *76*, 802.
(57) Yang, X.; Takada, K.; Itose, M.; Ebina, Y.; Ma, R.; Fukuda, K.; Sasaki, T. *Chem. Mater.* **2008**, *20*, 479.
(58) Bianconi, A.; Garcia, J.; Benfatto, M. In *Synchrotron Radiation in Chemistry and Biology I*; Topics in Current Chemistry; Springer: Berlin, 1988; pp 29−67.
(59) Stöhr, J.; Sette, F.; Johnson, A. L. *Phys. Rev. Lett.* **1984**, *53*, 1684.
(60) Haas, O.; Vogt, U. F.; Soltmann, C.; Braun, A.; Yoon, W.-S.; Yang, X. Q.; Graule, T. *Mater. Res. Bull.* **2009**, *44*, 1397.
(61) Haas, O.; Ludwig, C.; Bergmann, U.; Singh, R. N.; Braun, A.; Graule, T. *J. Solid State Chem.* **2011**, *184*, 3163.
(62) Blasco, J.; Aznar, B.; García, J.; Subías, G.; Herrero-Martín, J.; Stankiewicz, J. *Phys. Rev. B: Condens. Matter Mater. Phys.* **2008**, *77*, 054107.
(63) Klaus, S.; Cai, Y.; Louie, M. W.; Trotochaud, L.; Bell, A. T. manuscript in preparation, 2015.
(64) Wang, L.; Maxisch, T.; Ceder, G. *Phys. Rev. B: Condens. Matter Mater. Phys.* **2006**, *73*, 195107.
(65) García-Mota, M.; Bajdich, M.; Viswanathan, V.; Vojvodic, A.; Bell, A. T.; Nørskov, J. K. *J. Phys. Chem. C* **2012**, *116*, 21077.
(66) Himmetoglu, B.; Floris, A.; de Gironcoli, S.; Cococcioni, M. *Int. J. Quantum Chem.* **2014**, *114*, 14.
(67) Szytula, A.; Balanda, M.; Dimitrijevi, Ž. *Phys. Status Solidi A* **1970**, *3*, 1033.
(68) Oleś, A.; Szytuła, A.; Wanic, A. *Phys. Status Solidi B* **1970**, *41*, 173.
(69) Nørskov, J. K.; Rossmeisl, J.; Logadottir, A.; Lindqvist, L.; Kitchin, J. R.; Bligaard, T.; Jónsson, H. *J. Phys. Chem. B* **2004**, *108*, 17886.
(70) Man, I. C.; Su, H.; Calle-Vallejo, F.; Hansen, H. A.; Martínez, J. I.; Inoglu, N. G.; Kitchin, J.; Jaramillo, T. F.; Nørskov, J. K.; Rossmeisl, J. *ChemCatChem* **2011**, *3*, 1159.
(71) Koper, M. T. M. *J. Electroanal. Chem.* **2011**, *660*, 254.
(72) Bajdich, M.; García-Mota, M.; Vojvodic, A.; Nørskov, J. K.; Bell, A. T. *J. Am. Chem. Soc.* **2013**, *135*, 13521.

DOI: 10.1021/ja511559d
J. Am. Chem. Soc. 2015, 137, 1305−1313